

Supplementary Information

Unusual Li-ion Storage through Anionic Redox Processes of Bacteria-driven Tellurium Nanorods

Min Gyu Kim^{a†*}, Dong-Hun Kim^{c†}, Taeyang Kim^b, Sunhwa Park^b, Gukyoung Kwon^b, Mi Sug Kim^a, Tae
Joo Shin^a, Hyungju Ahn^a, and Hor-Gil Hur^{b*}

^a*Pohang Accelerator Laboratory (PAL), Pohang 790-784, Republic of Korea*

^b*School of Environmental Science and Engineering, Gwangju Institute of Science and Technology (GIST),
Gwangju 500-712, Republic of Korea*

^c*Geologic Environment Division, Korea Institute of Geoscience and Mineral Resources, Daejeon 305-350,
Republic of Korea*

†These authors contributed equally to this work.

*Correspondence to: hghur@gist.ac.kr; mgkim@postech.ac.kr

Figure Captions (Figs. S1-S14)

Figure S1 | TEM galleries for the as-prepared *extracellular* Te nanorods and primary carbonizations under different conditions.

Figure S2 | TEM and SEM galleries for the as-prepared *intracellular* Te nanorods.

Figure S3 | TEM galleries for the primary carbonized *intracellular* Te nanorods under different heating conditions.

Figure S4 | Energy-dispersive X-ray analysis and thermogravimetric analysis (TGA) in comparison with that of *Shewanella oneidensis* MR-1. TEM images of *Shewanella oneidensis* MR-1 before and after heat treatment at 600 °C for 3hrs.

Figure S5 | Differential scanning calorimetric (DSC) analysis of as-prepared extra- and intracellular

telluriums and corresponding carbonized telluriums, in addition to *Shewanella oneidensis* MR-1.

Figure S6 | The discharge-charge voltage profiles of *Shewanella oneidensis* MR-1 and glucose carbonized at 600 °C for 3 h with current densities from 80 to 4000 mA g⁻¹.

Figure S7 | Rate performances of the as-prepared *extracellular* and *intracellular* Te nanorods.

Figure S8 | Rate performances of the carbonized *extracellular* Te nanorods above 1.0 V.

Figure S9 | Dependence of rate performances for *extracellular* Te nanorods on primary carbonization temperature and time.

Figure S10 | Voltage profiles and cycle properties of *intracellular* Te nanorods as a function of glucose amount.

Figure S11 | Simulated X-ray diffraction patterns for trigonal *P3₁21* and cubic *Fm-3m*

Figure S12 | *In situ* WAXD structural characterizations of amorphous *intracellular* Te.

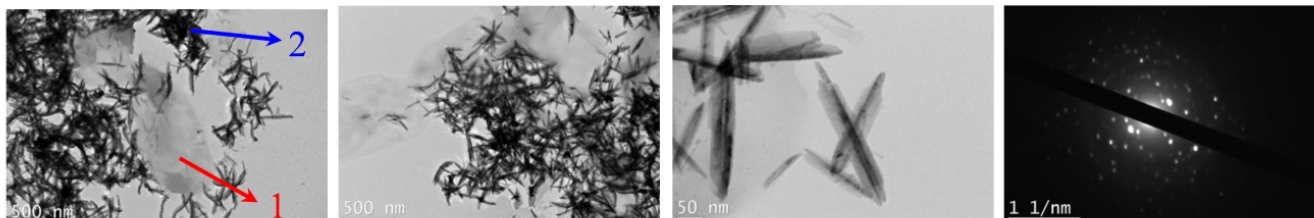
Figure S13 | Home-made *in situ* electrochemical cell for real-time XAFS structural characterizations and *in situ* setup at BL10C beamline.

Figure S14 | Differential capacity curves ($1/Q_0 * dQ/dV$) of as-prepared, primary-carbonized and glucose-driven *co*-carbonized extra- and intracellular telluriums, in addition to bulk metallic tellurium.

Supplementary comments

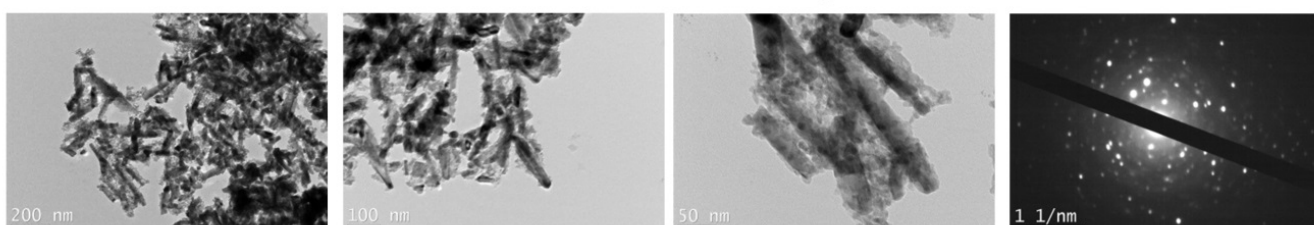
- 1) Interpretation of thermal analysis
- 2) Origin of different discharge-charge voltage profiles for intra- and extracellular nanorod
- 3) Possible Li-ion diffusion pathway

(A) As-prepared extracellular Te nanorods

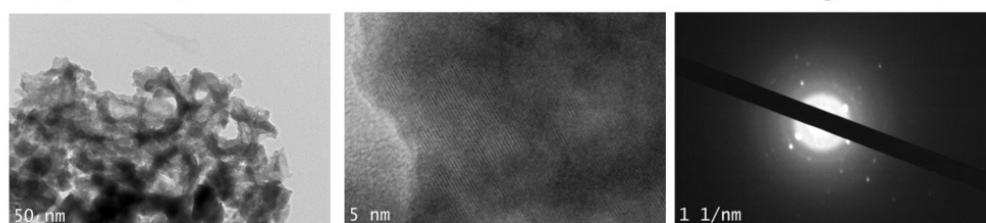


(1) *S. oneidensis* MR-1 bacterial cell and **(2) tellurium nanorods**

(B) Primary carbonization of extracellular Te nanorods @ 300°C, 6 h



(C) Primary carbonization of extracellular Te nanorods @ 600°C, 3 h



(D) Primary carbonization of extracellular Te nanorods @ 600°C, 6 h

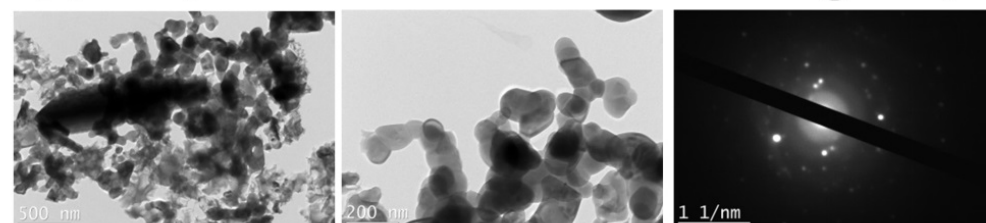
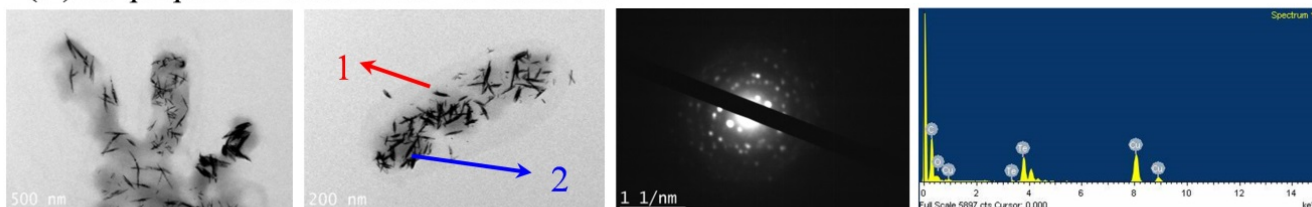


Figure S1 | TEM galleries for the as-prepared extracellular Te nanorods and primary carbonization under different conditions. TEM images for (A) as-prepared and primary carbonized Te materials at (B) 300 °C for 6 h, (C) 600 °C for 3 h and (D) 600 °C for 6 h in N₂ atmosphere with small area electron diffraction (SAED) patterns.

(A) As-prepared **intracellular** Te nanorods



(1) *S. oneidensis* MR-1 bacterial cell and (2) tellurium nanorods

(B) As-prepared **intracellular** Te nanorods

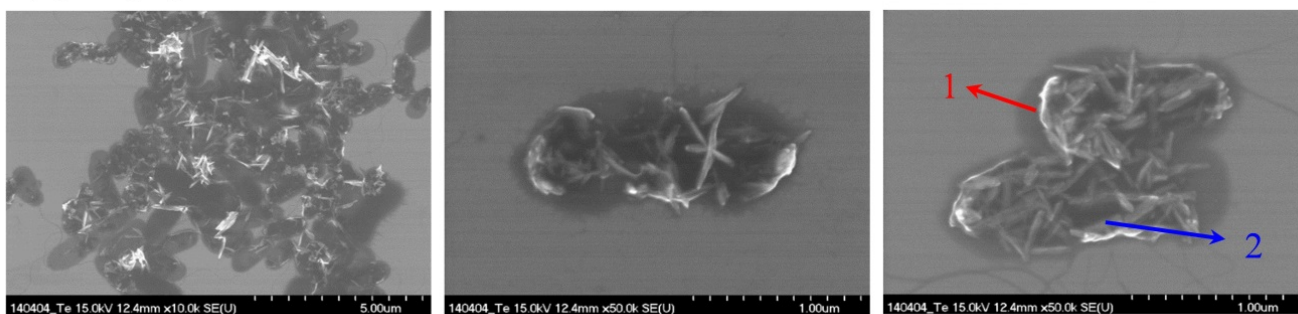
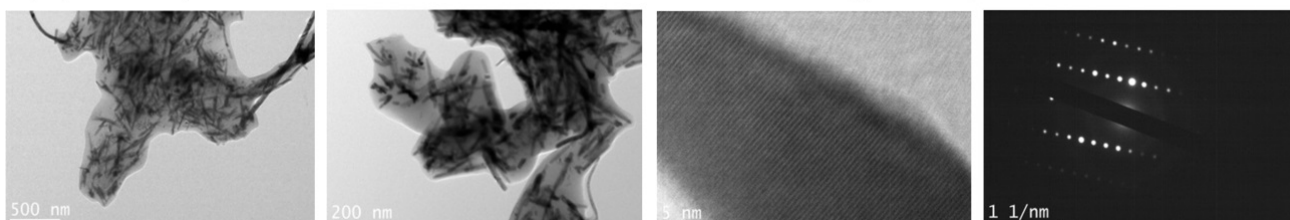
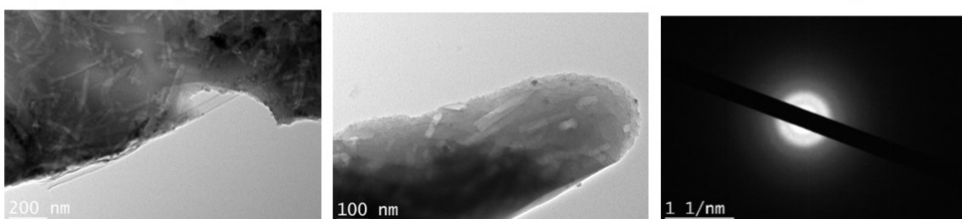


Figure S2 | TEM and SEM galleries for the as-prepared intracellular Te nanorods. (A) TEM images of as-prepared intracellular Te nanorods with SAED pattern and energy dispersive X-ray (EDX) spectroscopy (B) SEM images of as-prepared intracellular Te nanorods

(A) Primary carbonization of *intracellular* Te nanorods @300°C, 6 h



(B) Primary carbonization of *intracellular* Te nanorods @600°C, 3 h



(C) Primary carbonization of *intracellular* Te nanorods @600°C, 6 h

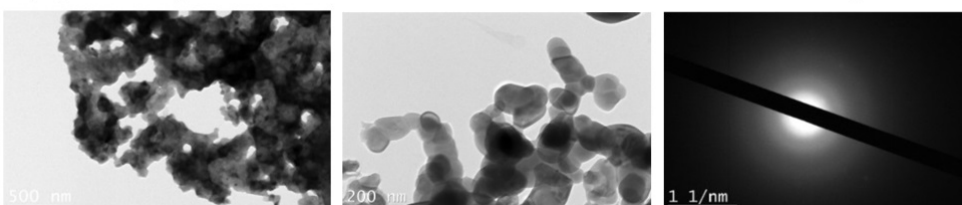


Figure S3 | TEM galleries for the primary carbonized *intracellular* Te nanorods under different heating conditions. TEM images for primary carbonized Te materials at (A) 300 °C for 6 h, (B) 600 °C for 3 h and (C) 600 °C for 6 h in N₂ atmosphere with SAED patterns.

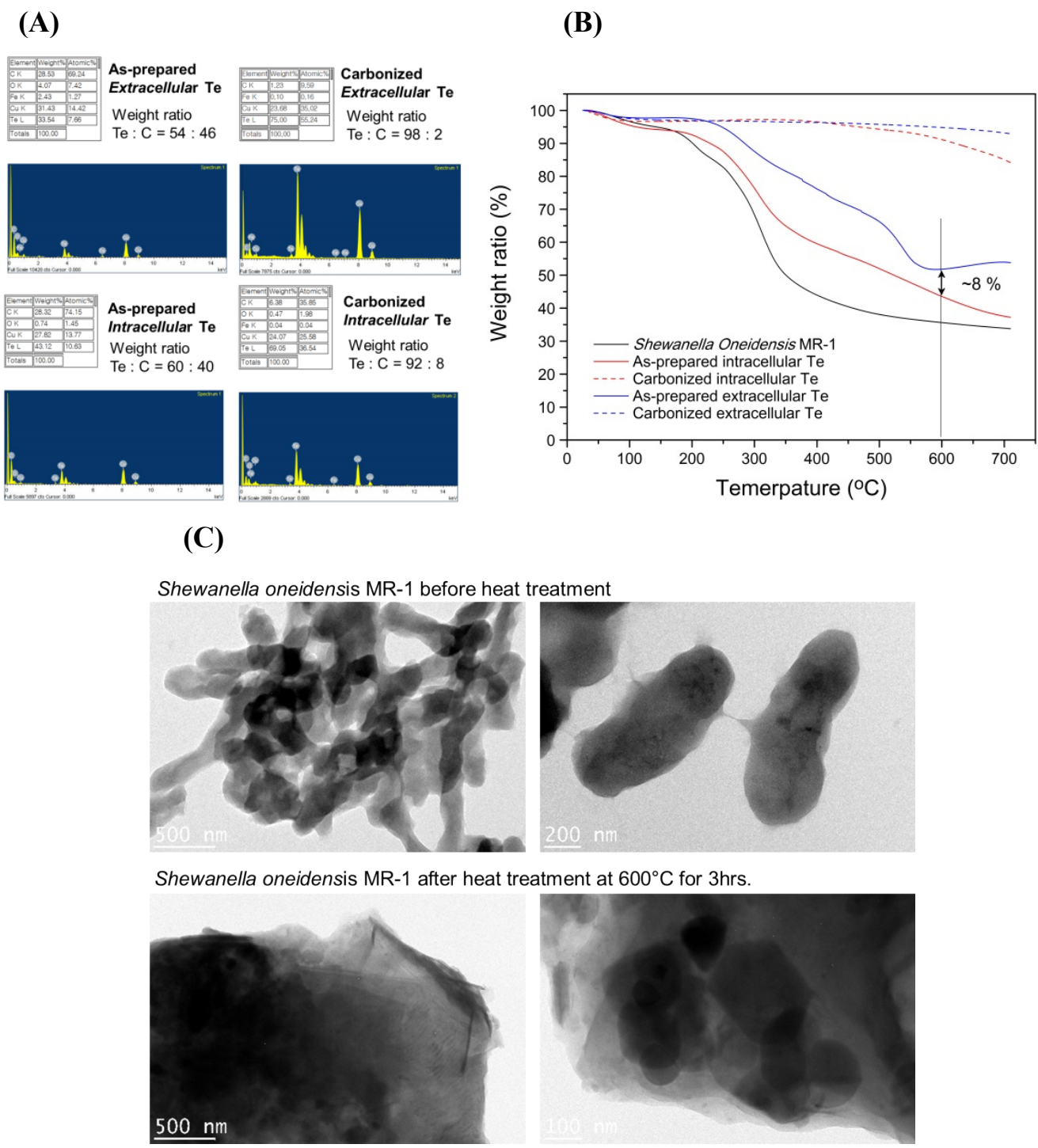


Figure S4 | (A) Energy-dispersive X-ray analysis and (B) thermogravimetric analysis (TGA) in comparison with that of *Shewanella oneidensis* MR-1. (C) TEM images of *Shewanella oneidensis* MR-1 before and after heat treatment at 600 °C for 3 h. TGA measurements were performed in N₂ flow on heating to 700 °C at a rate of 10 °C/min using a TG/DTA-6300 of Seiko thermogravimeter.

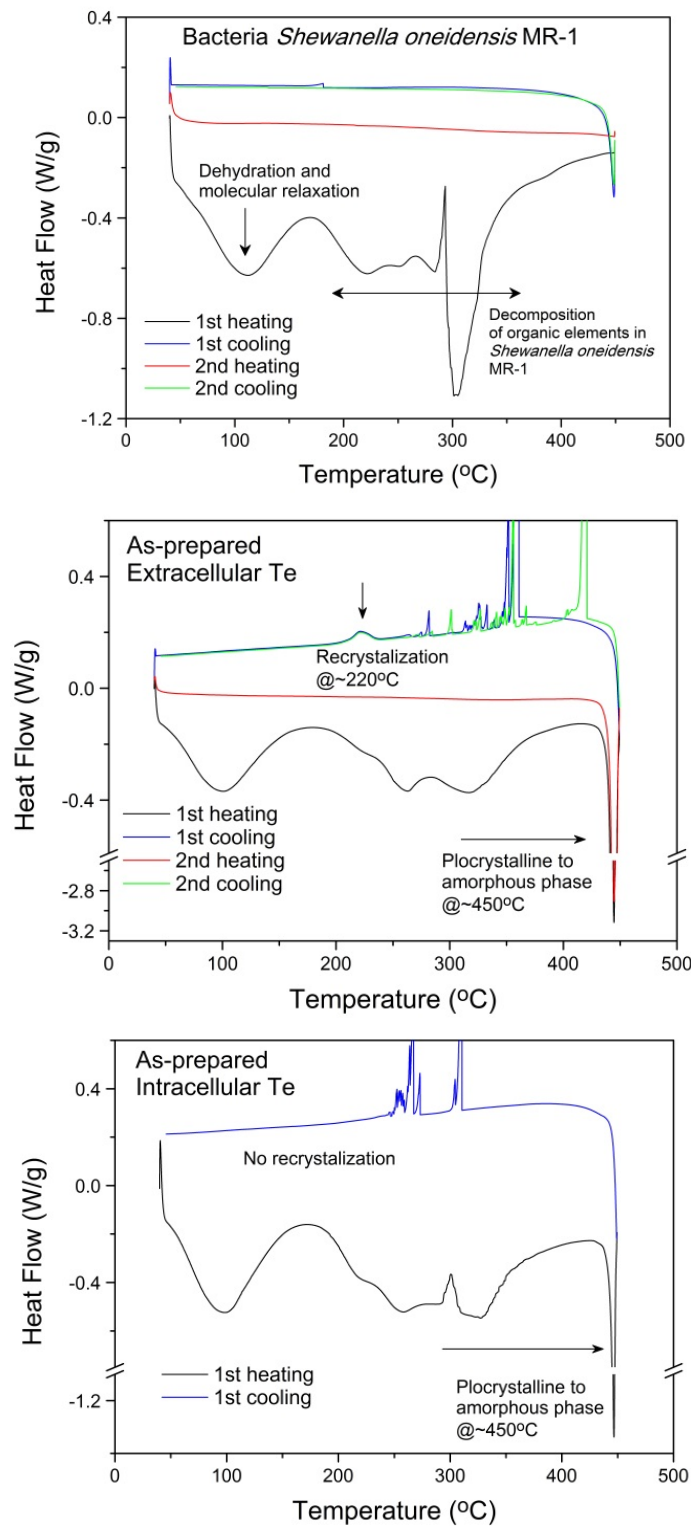


Figure S5 | Differential scanning calorimetric (DSC) analysis of as-prepared extra- and intracellular telluriums, in addition to *Shewanella oneidensis* MR-1. DSC measurements were performed in N₂ flow on heating to 450 °C at a rate of 10 °C/min using a DSC Q20 of TA Instruments. Unexpected signals in two as-prepared telluriums have been repeatedly observed case-by-case in several measurements. The signals seem to be due to mechanical stress of aluminum cell cover from outgassing of samples

1) Interpretation of thermal analysis

Our biologically-synthesized Te anode materials essentially includes the additional carbon from burning the bacterial cell. The capacity (mA h g^{-1}) by additional carbon from bacteria cannot be excluded from the total electrochemical performance. However, the carbon weights from bacteria-burning in the as-prepared extracellular and intracellular Te were not much high. The carbon amount could be estimated from energy-dispersive X-ray spectroscopy (EDX). The EDX analysis for the as-prepared extra- and intra-cellular Te before and after carbonization Te, present that the weight % ratio of carbon to tellurium change from initial high values of 46 and 40 weight % to 2 and 8 values, respectively. Of course, we acknowledge that the carbon weight ratio from the EDX cannot reflect overall carbon amount of the materials because the EDS depends on the selection of region and spot size. Nevertheless, the carbonization process commonly gives rise to much decrease of weight ratio of carbon to tellurium, compared to those of the initial as-prepared tellurium. For the glucose-driven co-carbonized Te, the weight % ratio of glucose to Te (glucose : Te = 1 : 10) was mechanically mixed before the co-carbonization. In general, it is well-known that the glucose is thermally-decomposed between 200 - 400°C and the weight decreases to 10% at 600°C. (*J. Mater. Chem. A*, 2014, 2, 19324-19329) In this study, the 10% weight addition of initial glucose with respect to the original tellurium can be simply estimated to be decomposed to nearby 1%. Therefore, the total amount of carbons in the carbonized Te can be speculated to be below 10%. The carbon amounts in the present study are relatively little, compared to ~50% of Te/Carbon composite (*J. Mater. Chem. A*, 2014, 2, 12201-12207., Ref 35 in this manuscript) and ~30% of Tellurium@Ordered Macroporous Carbon Composite materials (*Adv. Energy Mater.*, 2015, 5, 1401999., Ref. 36). These results can be supported with TGA analysis. At 250 °C, the as-prepared extra- and intracellular Te start to show meaningful weight loss and result in weight loss higher than 50% at 600 °C. On the other hand, the carbonized Te nearly show constant weight although the carbonized intracellular Te shows a slight weight loss at 600 °C. Therefore, it can be considered that this severe weight losses in the as-prepared telluriums result from the decomposition of organic elements in the bacteria. The weight loss can be also supported with differential scanning calorimetry (DSC)

On heating, commonly, all samples show thermal behavior for dehydration below 200 °C. The as-prepared telluriums also commonly present a broad endothermic peak feature between 200 °C and 400 °C. The broad thermal behavior corresponds to the thermal decomposition of organic elements in the bacteria *S. oneidensis* MR-1, which results in severe weight loss in TGA analysis. The strong endothermic peak closed to 450 °C can be assigned to phase transition from polycrystalline to amorphous phase by melting of Te. On cooling, the as-prepared intracellular Te does not show any effective exothermic peak, while the as-prepared extracellular gives an exothermic peak nearby 220 °C corresponding to recrystallization. The fact means that the as-prepared intracellular Te changes to amorphous phase after heating, while the as-prepared extracellular Te keeps reversibly polycrystalline phase. Also, once carbonized, the carbonized intracellular Te with initially amorphous phase gives no endothermic peak at ~450 °C, while the carbonized extracellular Te shows reversible endothermic and exothermic peaks for phase transitions from polycrystalline to amorphous and vice versa, respectively. These thermal analyses are in good agreement with XRD and small

area electron diffraction results in the manuscript

As a result, we do not exclude the contribution of intrinsic carbon phase from the organic bacteria on the capacity (mA h g^{-1}). The contribution on capacity is very small due to the severe weight loss during heating. But we agree that the carbon phase promotes the cycle life and rate capability of bacteria-driven Te anode materials as mentioned above

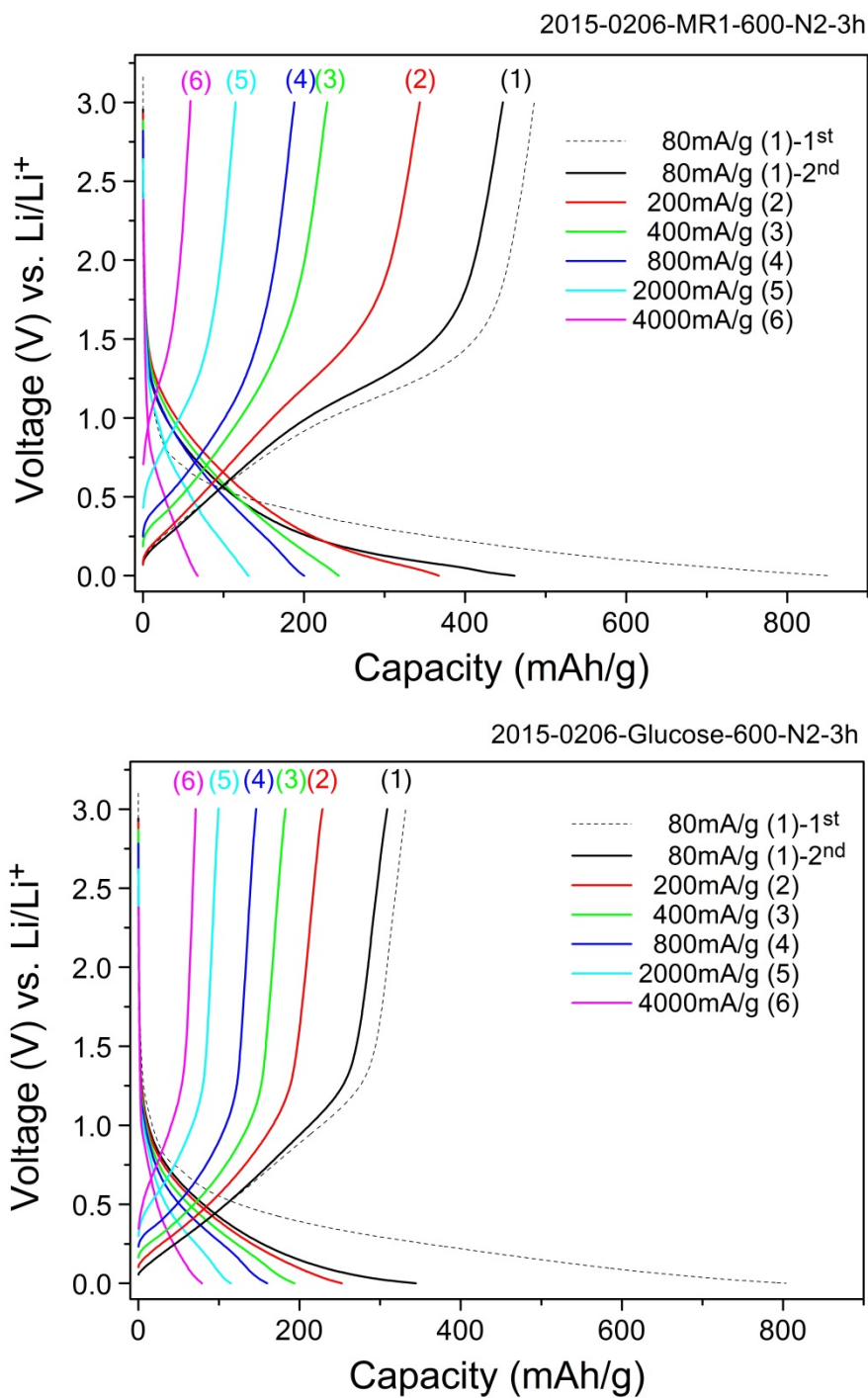
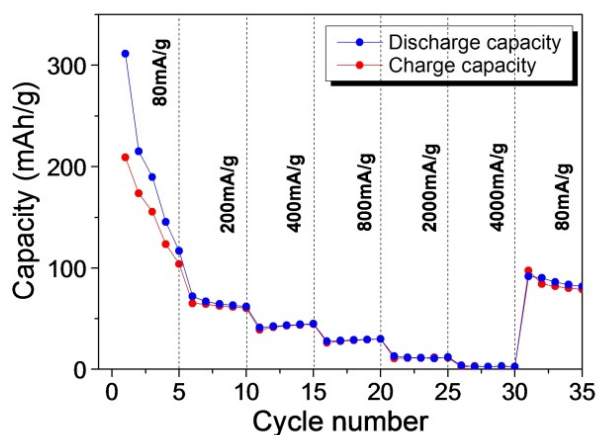
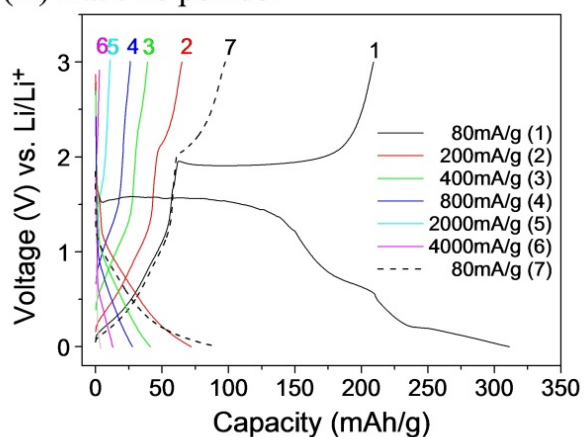
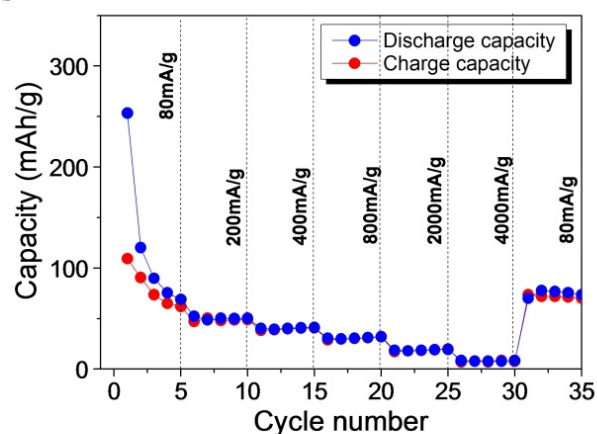
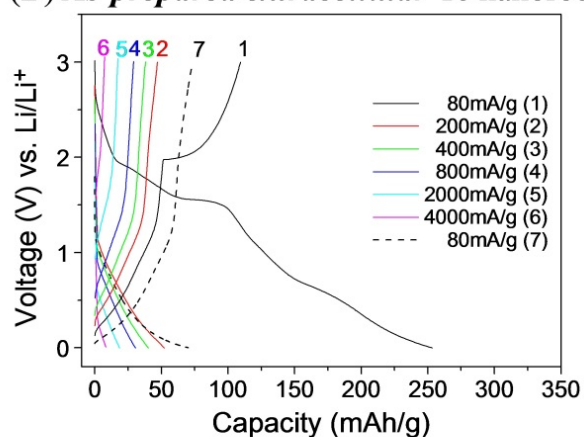


Figure S6 | The discharge-charge voltage profiles of *Shewanella oneidensis* MR-1 and glucose carbonized at 600 °C for 3 h with current densities from 80 to 4000 mA g⁻¹.

(A) **Bulk** Te powder



(B) **As-prepared extracellular** Te nanorods



(C) **As-prepared intracellular** Te nanorods

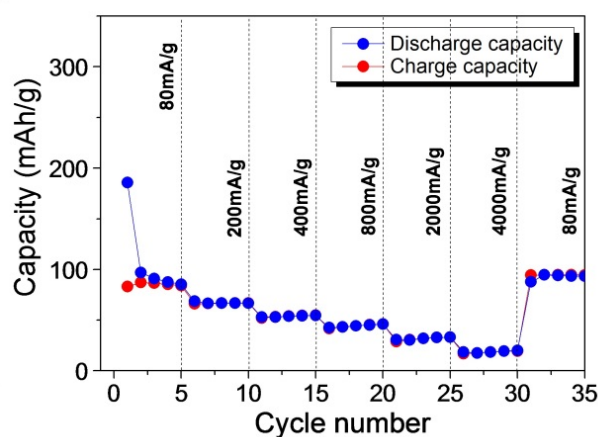
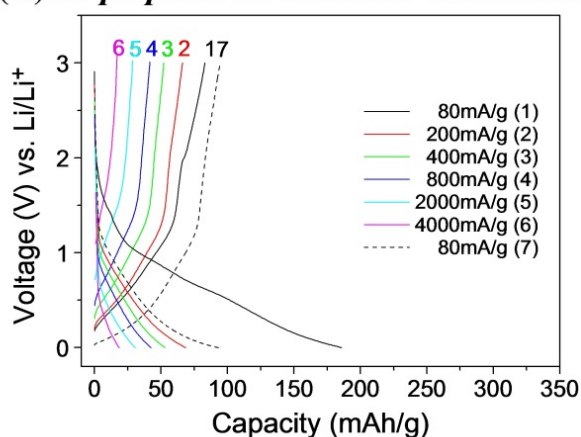
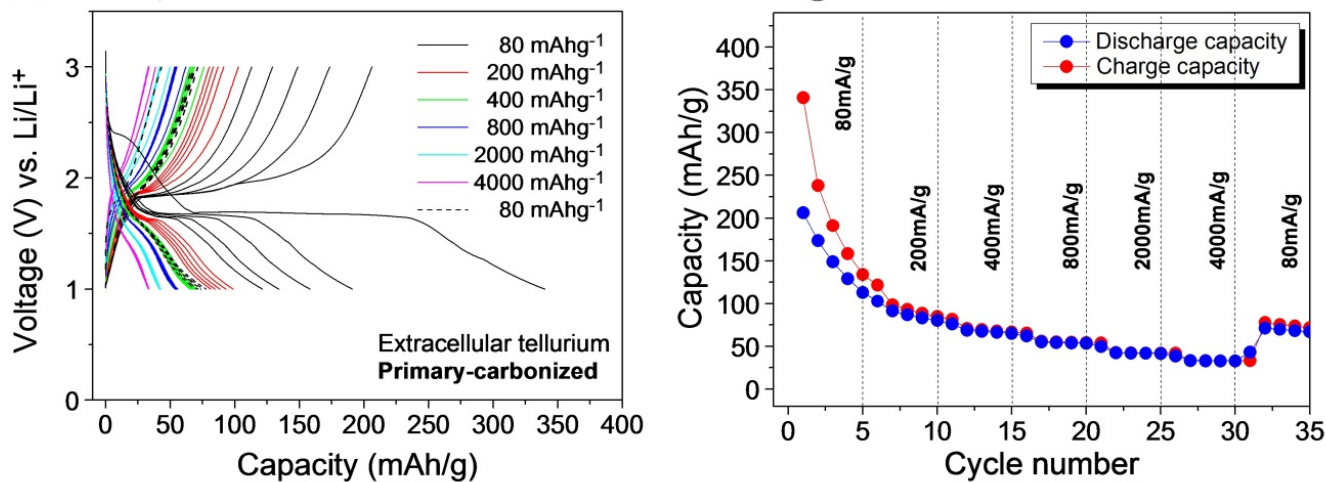


Figure S7 | Rate performances of the as-prepared *extracellular* and *intracellular* Te nanorods. The discharge-charge voltage profiles of (A) Te *bulk* powder, (B) the as-prepared *extra*- and (C) *intracellular* Te nanorods with various current densities from 80 mA g⁻¹ to 4000 mA g⁻¹. The Rate capabilities have been tested with 5 cycles in each current density.

(A) Primary carbonization of *extracellular* Te nanorods @600°C, 3 h



(B) Glucose-assisted *co*-carbonization of *extracellular* Te nanorods @ 600°C, 3 h

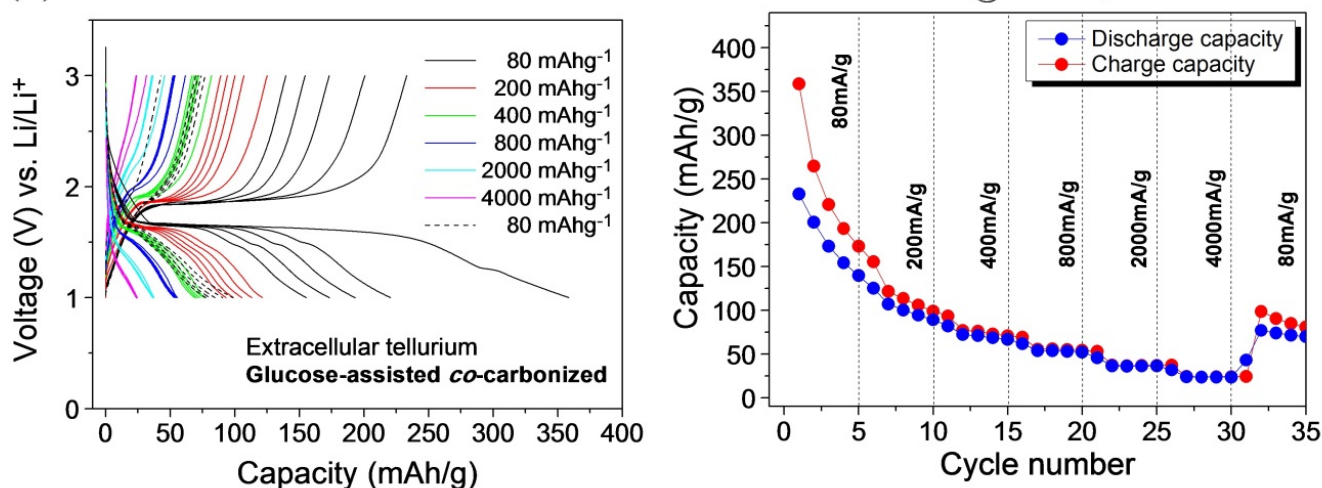
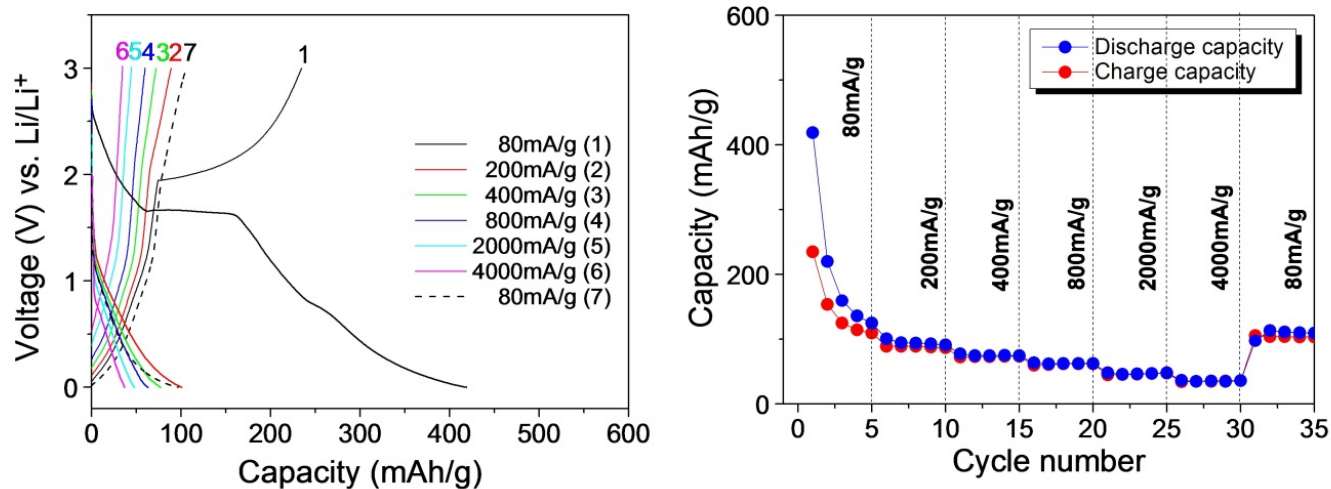


Figure S8 | Rate performances of the carbonized *extracellular* Te nanorods above 1.0 V. The discharge-charge voltage profiles of (A) the primary carbonized and (B) the glucose-driven *co*-carbonized Te nanorods at 600 °C for 3 h with various current densities from 80 mA g^{-1} to 4000 mA g^{-1} in the voltage windows between 1.0 and 3.0 V. The rate capabilities have been tested with 5 cycles in each current density.

(A) Primary carbonization of extracellular Te nanorods @ 300 °C, 6 h



(B) Primary carbonization of extracellular Te nanorods @ 600 °C, 6 h

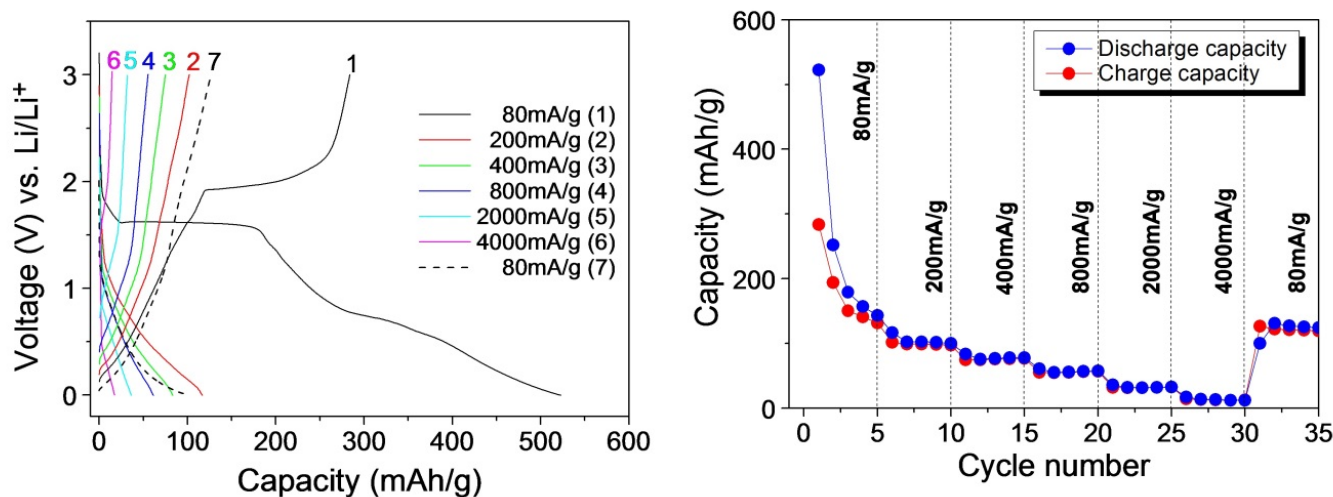
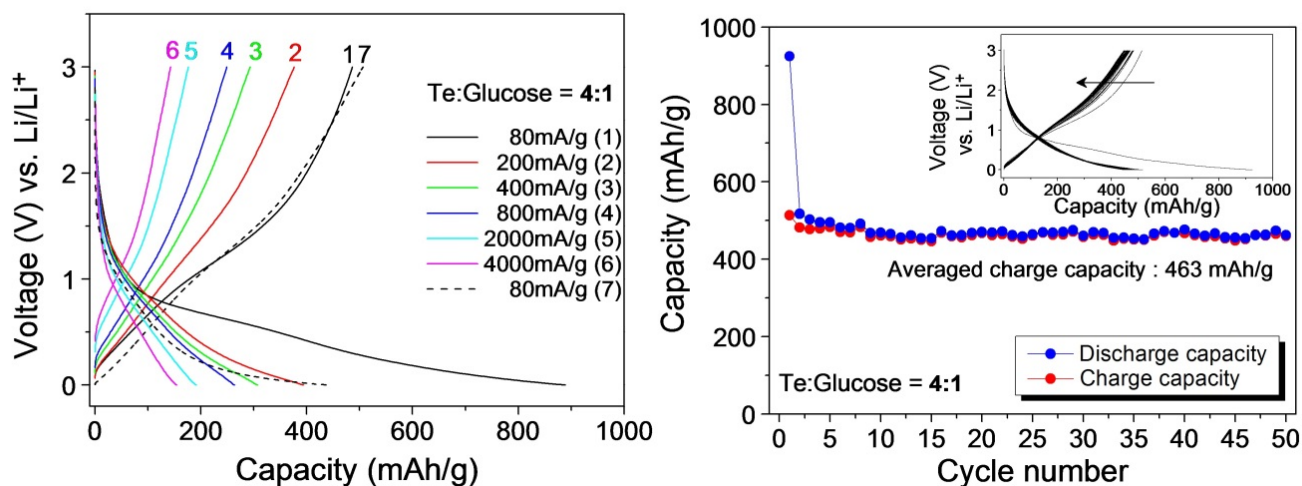


Figure S9 | Dependence of rate performances for *extracellular* Te nanorods on primary carbonization temperature and time. The discharge-charge voltage profiles and rate capabilities of primary-carbonized extracellular Te nanorods at (A) 300 °C and (B) 600 °C for 6 h with various current densities from 80 mA g⁻¹ to 4000 mA g⁻¹. The rate capabilities of primary-carbonized telluriums have been tested with 5 cycles in each current density.

(A) Weight ratio of *intracellular* Te nanorods to glucose (4:1)



(B) Weight ratio of *intracellular* Te nanorods to glucose (2:1)

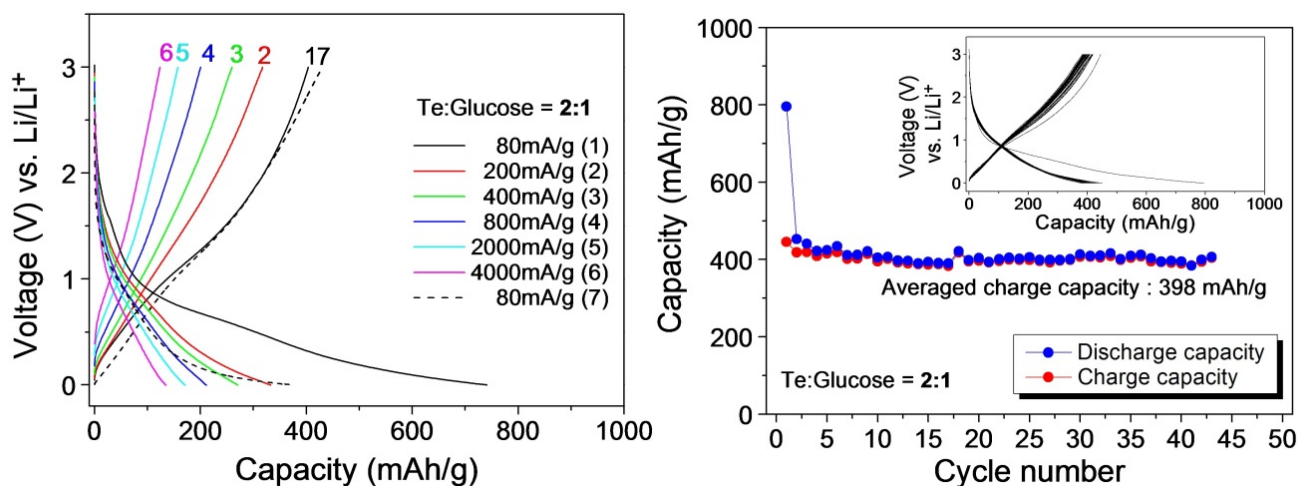


Figure S10 | Voltage profiles and cycle properties of *intracellular* Te nanorods as a function of glucose amount. The discharge-charge voltage profiles of the glucose-driven *co*-carbonized *intracellular* Te for the weight ratio of Te to glucose, (A) 4:1 and (B) 2:1 under various current densities from 80 mA g⁻¹ to 4000 mA g⁻¹. Rate capabilities of glucose-driven *co*-carbonized Te for 5 cycles in each current density. Also, the discharge and charge capacities of the Te have been tested on 50 cycles with current density of 80 mA g⁻¹. Each inset figure presents all 50-cycled voltage profiles.

2) Origin of different discharge-charge voltage profiles for intra- and extracellular nanorod

At a glance, basically, the different voltage profiles for intra- and extracellular nanorods are originated from their polycrystalline and amorphous structures. Here, the origin for the evolution of different phases can be at first helpful to suggest the cause of the different voltage profiles.

The difference between intra- and extracellular Te is simply that Te nanorods exist inside and outside bacterial cell, respectively. From XRD and small area electron diffraction, it is clear that two Tes before heating have commonly polycrystalline phase. Based on the clear phase dependence of intra- and extracellular nanorods on the heating, a reasonable origin for different voltage profiles can be inferred in the viewpoint of structure. For the extracellular nanorods with polycrystalline phase (the total 3.8 mole Li-ion storage), the Li-ion can be initially diffused into the empty space between every single interchain in Te atomic wire bundle and then Li_2Te -like phase formation. This structural variation could be reflected in the plateau region at ~ 1.6 V, which can be supported with *in situ* WAXD study. In the next discharge to 0.01 V after 2 mole Li-ion storage, the broad discharge profile represents additional 1.8 mole Li-ion storage to Li_2Te -like phase. In the voltage region, interestingly, the effective and gradual XANES spectra shows spectral characteristic for more reduced Te, which can support the simple Li-ion accumulation around tellurium anions. On the other hand, the intracellular nanorods with amorphous phase (the total 5.2 mole Li-ion storage) don't show any plateau region at ~ 1.6 V, meaning no phase transition to Li_2Te . Therefore, a single broad voltage profile of the intracellular nanorods can be considered to be originated from the simple Li-ion accumulation around Te promoted by anionic redox process. The fact can be supported with gradual evolution of more reduced XANES spectral characteristics up to 0.01 V.

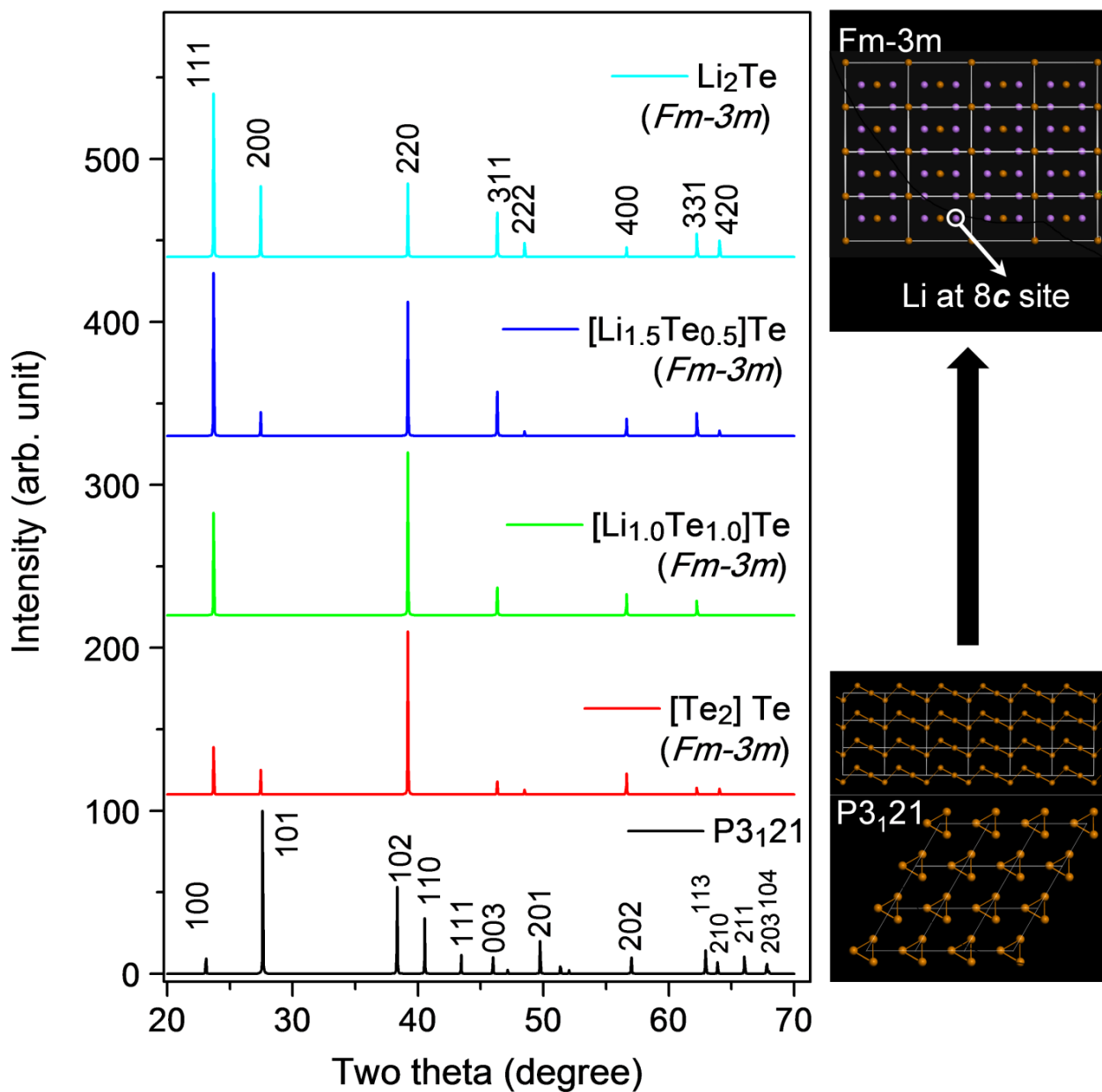


Figure S11| Simulated X-ray diffraction patterns for trigonal $P3_121$ and cubic $Fm-3m$. Various XRD patterns have been calculated with different mole ratios of Te to Li in $8c$ site of space group $Fm-3m$ in Li_2Te cubic phase where Te is positioned into $4a$ site (0,0,0) and Li into $8c$ site (0.25, 0.25, 0.25).

3) Possible Li-ion diffusion pathway

Experimental determination for Li-ion intercalating pathway into lattice position is physically difficult due to extremely light X-ray scattering power by low electron density. In this manuscript, we suggested plausible Li-ion diffusion pathway into empty space between interchains of Te atomic wires. Since the lithiation leads to Li_2Te phase, the variation of crystal structure results in Te atomic rearrangement from helically zigzagging ordering to flat zigzag ordering by Li-ion binding. For the phosphorene with similar zigzagging atomic ordering, diffusion behaviors of Li-ion have been recently reported based on the density functional theory (DFT) calculations. [W. Li, Y. Yang, G. Zhang, Y. W. Zhang, Ultrafast and directional diffusion of lithium in phosphorene for high-performance lithium-ion battery. *Nano Lett.* (2015). (In press, DOI: 10.1021/nl504336h)] Suggesting two possible Li-ion diffusion pathways with *so-called* armchair diffusion and zigzag direction, they figured out that the zigzag direction is much energetically favorable to easy and fast Li-ion conduction with lower energy barrier of Li-ion diffusion. Although the crystal structure is not perfectly identical to each other, the recent DFT calculations can provide an opportunity of Li-ion diffusion into the empty space in the Te atomic wire bundles. They also reported that the diffused Li exists in cationic state, which leads to semiconducting to metallic transition of phosphorene by conducting electron distribution in the phosphorene layer.

Similar interpretation can be introduced to Te nanorod. The Li-ion diffusion along to zigzagging direction gives rise to formation of anionic tellurium (telluride) including electron. Here, Li-ion binding with telluride leads to $\text{Li}^+\text{-Te}_n^{2-}$ ion pair with Coulombic interactions. As indirect experimental evidence, the lithiation show decrease of FT peak intensities for Te-Te intrachain and interchain in radial distribution function for EXAFS spectra. The spectral change can be explained with decrease of static disorder by Te-Te/Li bonding.

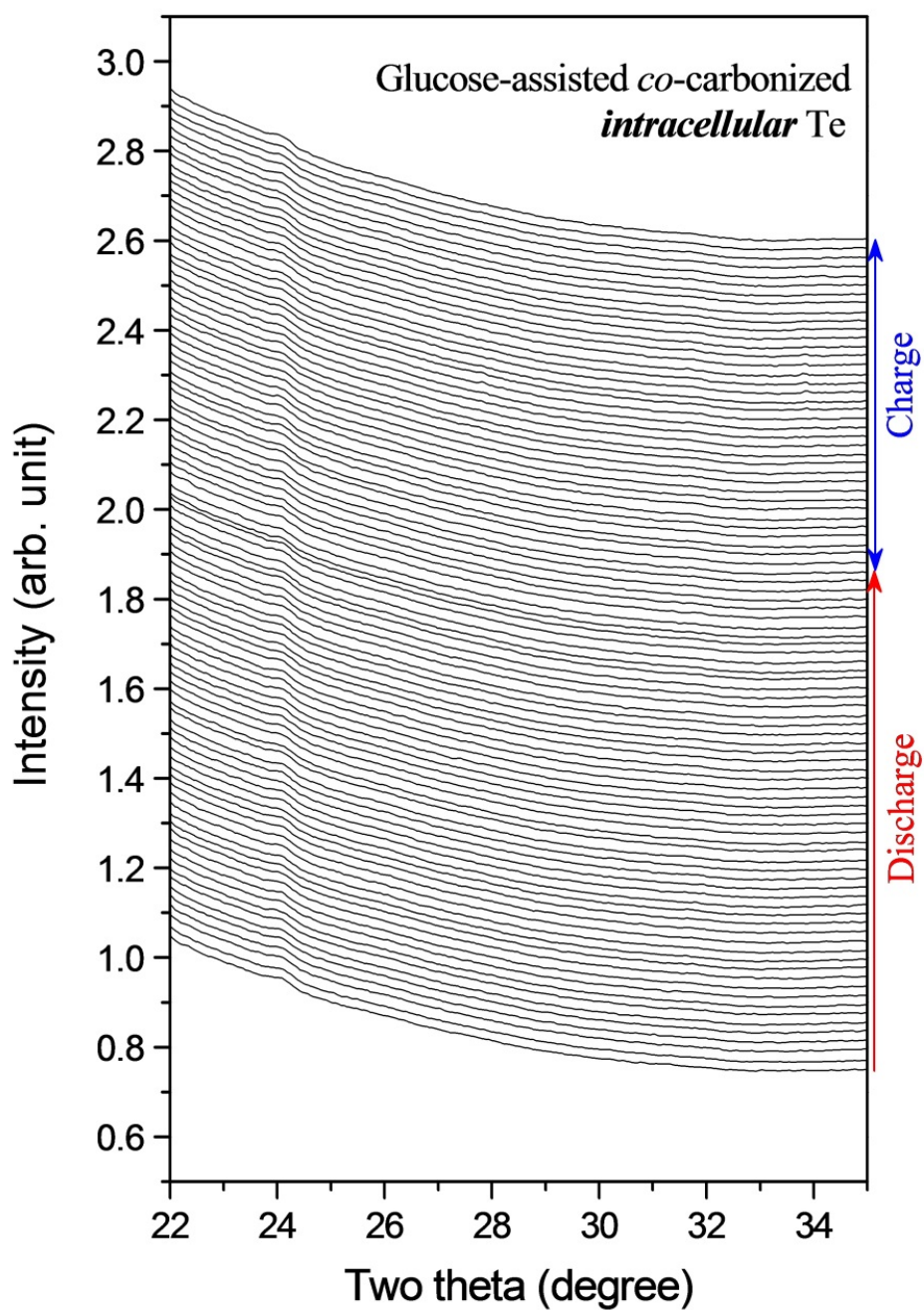


Figure S12 | *In situ* WAXD structural characterizations of amorphous intracellular Te. *In situ* wide-angle X-ray diffraction patterns for the glucose-driven intracellular Te (amorphous phase) were observed during the 1st discharge-charge process. Unlike the glucose-driven extracellular Te showing the polycrystalline phase, the amorphous phase keeps constant over the 1st cycle.

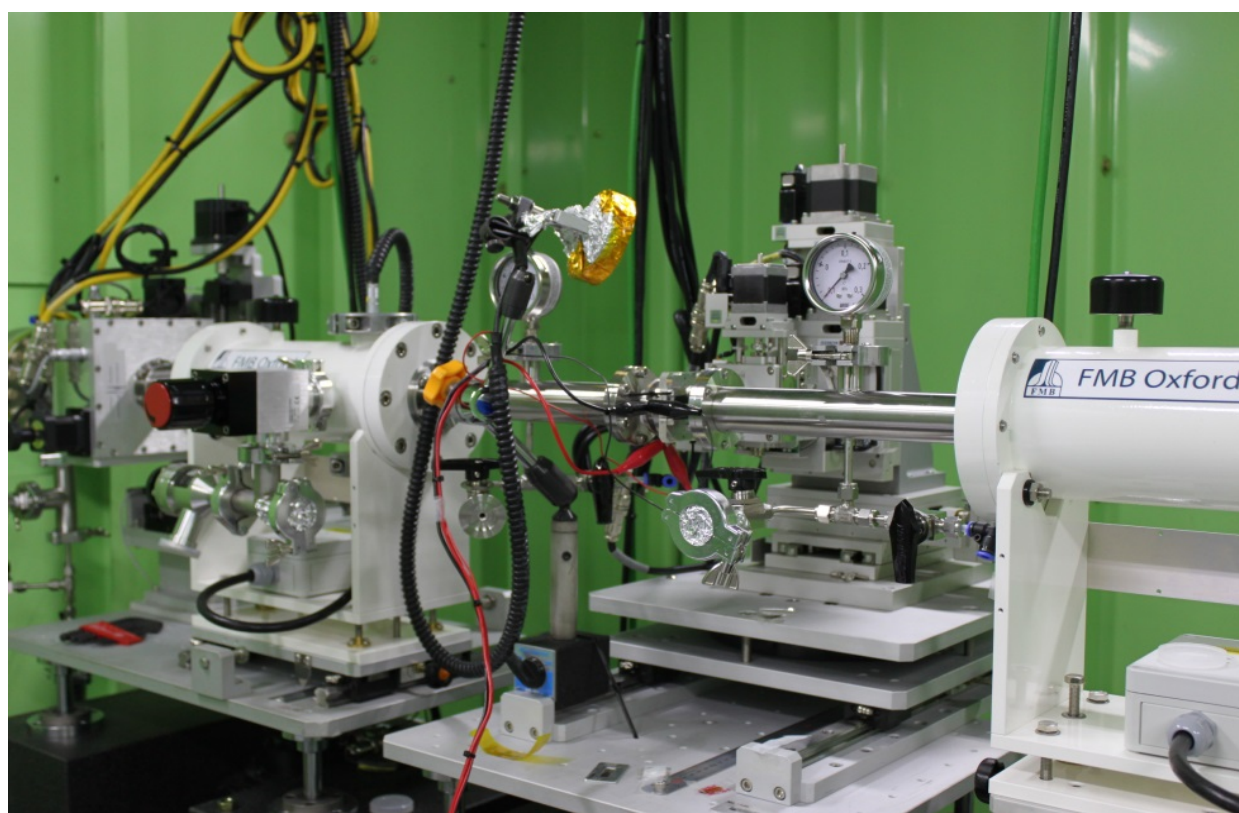
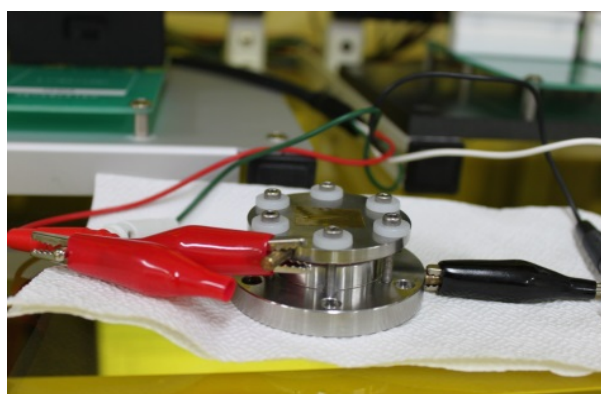


Figure S13 | Home-made *in situ* electrochemical cell for real-time XAFS structural characterizations and *in situ* setup at BL10C beamline. Real-time Te K-edge X-ray absorption spectroscopic data during discharging and charging processes have been recorded for the Te electrode assembled with home-made *in situ* electrochemical cell with polyimide film windows (Swagelok-type cell)

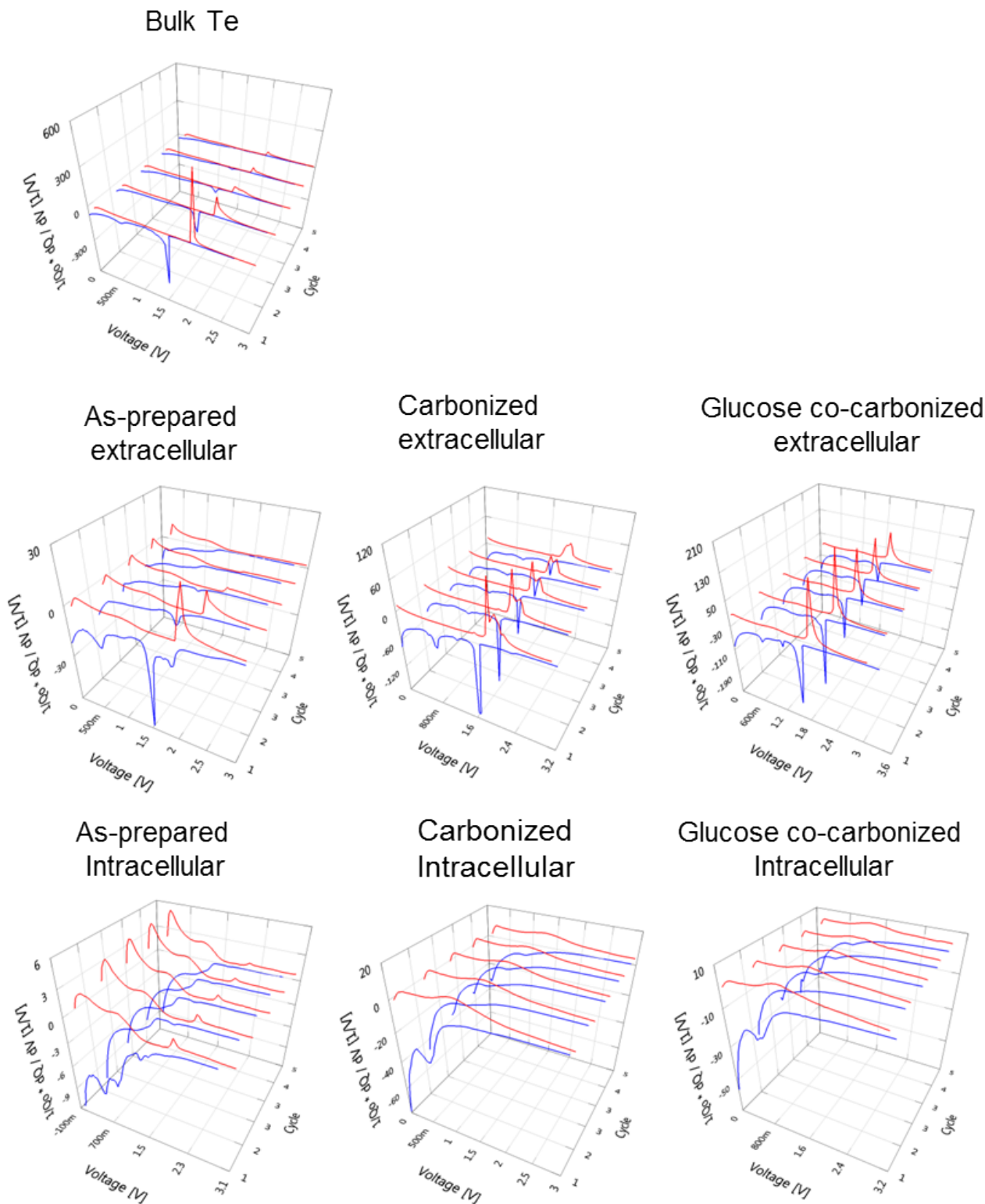


Figure S14 | Differential capacity curves ($1/Q_0 \cdot dQ/dV$) of as-prepared, primary-carbonized and glucose-driven *co*-carbonized extra- and intracellular telluriums, in addition to bulk metallic tellurium. Each data shows the differential capacity curves of first five cycles measured with current rate of 80 mA g⁻¹.